

Annual Review of Condensed Matter Physics

Focused Ion Beam Microstructuring of Quantum Matter

Philip J.W. Moll

Microstructured Quantum Matter Group, Max Planck Institute for Chemical Physics of Solids,
D-01187 Dresden, Germany; email: moll@cpfs.mpg.de

Annu. Rev. Condens. Matter Phys. 2018. 9:147–62

First published as a Review in Advance on
December 8, 2017

The *Annual Review of Condensed Matter Physics* is
online at conmatphys.annualreviews.org

<https://doi.org/10.1146/annurev-conmatphys-033117-054021>

Copyright © 2018 by Annual Reviews.
All rights reserved

Keywords

focused ion beam, FIB, quantum materials, mesoscale, superconductivity, microfabrication

Abstract

Focused ion beam (FIB) machining promises exciting new possibilities for the study of quantum materials through precise control over the shape and geometry of single crystals on the submicrometer scale. It offers viable routes to fabricate high-quality mesoscale structures from materials that cannot yet be grown in thin-film form and to enhance the experimentally accessible signatures of new physical phenomena. Prototype devices can also be produced in a silicon-chip environment to investigate directly the materials application potential for future electronics. This review introduces the concepts of ion beam shaping of matter, discusses the role and extent of surface damage and material disorder inherent to these techniques, and gives an overview of recent experiments on FIB-structured crystals. Given the early stage of the field of FIB-fabricated quantum materials, much is yet to come, and emergent trends and future directions are also discussed.

1. INTRODUCTION AND IMPACT

Quantum matter describes a broad class of materials where quantum mechanics manifests itself in unusual ways and induces novel electronic behavior. However, experiments are often limited by the size and shape of available crystallites, especially in newly discovered compounds. An emerging trend in the field employs focused ion beam (FIB)-based techniques to control the shape of such crystals on the submicrometer level. FIB-cut crystals can be tailored specifically to suit the requirements of a given experiment. The FIB has already proven invaluable in the research of quantum materials, yet most of its potential to advance experimental research remains to be explored. The basic operating principle is based on a highly focused beam of ions, impacting on a nanometer-sized spot and locally sputtering the target crystal.

Aligned crystalline samples can be selectively carved from polycrystals, microcrystallites, and powders. Thus, measurements of crystalline properties such as the orientation dependence of electric transport coefficients become also possible in materials in which no macroscopic single crystals exist. Even when large crystals are available, FIB structuring is a promising approach to access mesoscale physics in materials where no thin films of quality comparable to that of single crystals are available.

This review first discusses a set of examples of previous applications of FIB micromachining approaches in quantum matter research. It then discusses the technique's potential and contrasts the advantages and disadvantages of the FIB process, in particular the key issues of surface modification and damage due to ion irradiation. The final aim is to provide a good toolbox and starting set of procedures for readers interested in starting their own microstructuring projects.

1.1. Applications of Focused Ion Beam in Condensed Matter Physics

Electron beams were recognized early in the past century for their high potential in analytical and imaging applications in electron microscopy. Following from that, the idea emerged to manipulate matter on the nanoscale by using ion beams, as the heavier and more energetic ions strongly interact with a sample. Pioneering work up to the 1970s followed field emission microscope designs using solid sources as well as gas ionization sources, yet the low brightness of these sources and time stability issues hindered their larger-scale application. Invention of the liquid metal ion source (LMIS) in 1975 (1) and its subsequent incorporation into a scanning ion microscope in 1979 (2) formed the foundation of the modern FIB. This source technology offers self-sharpening tips from liquid metals, which act as position-stable sources at high brightness. The basic operating principle is the self-formation of a cone-like tip called the Taylor cone as a solution for hydrostatic equations balancing the forces of surface tension and applied electric field. Whereas LMISs have been shown for various metals, the commercial FIB instrument market is focused on gallium (Ga) for the convenience of its low melting point. Reference 3 provides a good historical and technological perspective on technical FIB developments, and Reference 4 is a didactical introduction into source and lens technology.

Today, the FIB has become an invaluable tool for microanalysis and microstructuring. Its predominant field of application is the semiconductor industry, where it is used for failure analysis and quality control of microchips on the single transistor level. In universities, it is a workhorse in material science for analytical purposes and the preparation and thinning of specimens for transmission electron microscopy (TEM) (5). Further interesting microfabrication applications include the study of mechanical defect propagation in micropillar compression experiments (6) and mesoscale structures in the context of photonic crystals (7). Recently, three-dimensional (3D) reconstructed images obtained from FIB tomography have become a growing trend in biological applications (8).

FIB machining is also a simple approach for fabrication of microstructures from crystalline material for electric and magnetic measurements. For example, with the discovery of strongly anisotropic cuprate high-temperature superconductors, FIB machining was used to make early microdevices. The main application was the fabrication of interlayer transport devices and intrinsic Josephson junction “mesa structures” as terahertz emitters (9–11) as well as Josephson junctions and SQUIDs (12, 13). A key advantage of FIB microprocessing as a kinetic technique is the relative ease with which one can work on chemically different compounds. It has been employed in the development of numerous novel mesoscale devices such as bismuth-based scanning hall sensors (14), nanoscale capacitors (15, 16), nanoscopic scanning four-probe resistance heads (17), skyrmion microbars (18), and graphene-nanoribbon-based photodetectors (19).

Precise control over the crystal shape makes FIB machining also useful for improving measurements of thermodynamic quantities such as magnetization. In particular, it has been employed to study Sr_2RuO_4 , a candidate material for chiral p-wave superconductivity. Here the chiral nature of the order parameter is expected to lead to spontaneous edge currents that appear as an anomalous magnetization in the Meissner state of the superconductor. To observe a measureable magnetization from a sample, high-purity crystals were machined into micrometer-sized samples. These were successfully coupled to cantilevers (20) and conventional SQUID magnetometers (21) to detect the small magnetization or magnetic torque of these samples. FIB fabrication is also a promising route to fabricate Josephson junctions and flux ring structures from Sr_2RuO_4 (22–24) and to fabricate tunnel junctions on pristine cleaved crystallites (25).

Figure 1 provides an exemplary overview of experiments based on FIB microstructuring, and highlights the versatility of the fabrication technique. It further highlights how creative use of FIB processing leads to crystalline devices that enable direct access to the physics of these quantum materials, including precise contacts for small crystallites, crystalline transport devices, graphene devices on the 100-nm scale, and designer crystals for torque magnetometry.

1.2. Iron-Based Superconductors

The in situ capability of the FIB to deposit metals for electric contacts and to micromachine make a powerful combination for fabricating electric devices from microcrystallites, especially when their shape and size defy traditional means of lithographic or manual contact fabrication (**Figure 1a**). Soon after the initial reports of superconductivity in iron-based superconductors, the “1111” class of REFeAsO ($\text{RE} = \text{rare earth}$) were identified as hosting the highest T_c among the iron arsenides, and still GdFeAs(O,F) holds the record with $T_c \sim 56$ K. Yet, most experimental work is focused on families with lower T_c , such as BaFe_2As_2 ($T_c \sim 36$ K) or FeSe ($T_c \sim 8$ K) (see, e.g., 30). Single crystals of record T_c oxides are difficult to grow and usually appear in the form of crystallite platelets, with diameters on the $<100\text{-}\mu\text{m}$ scale. Early on, the pioneering work in Reference 31 showed the FIB is ideally suited for the study of such microcrystallites, thereby establishing its basic superconducting properties such as their low anisotropy of the upper critical field (26). Similarly shaped microparticles of SmFeAs(O,H) (32), $\text{Pr}_4\text{Fe}_2\text{As}_2\text{Te}_{1-x}\text{O}_4$ (33), and $\text{Sm}_4\text{Fe}_2\text{As}_2\text{Te}_{1-x}\text{O}_{4-y}\text{F}_y$ (34) have been studied successfully using FIB contact fabrication.

In further studies researchers were able to control the crystal shape in three dimensions, leading to the development of devices designed for experiments investigating specific physical issues. One key question concerns the role of electronic anisotropy in attaining high-temperature superconductivity. Both cuprates and iron-arsenides are electronically layered materials, which hinted toward the importance of two-dimensionality for high T_c , for example, through the more pronounced divergence of electronic susceptibilities. Therefore, experiments probing transport anisotropy in the normal as well as superconducting state were required, yet these were hindered by

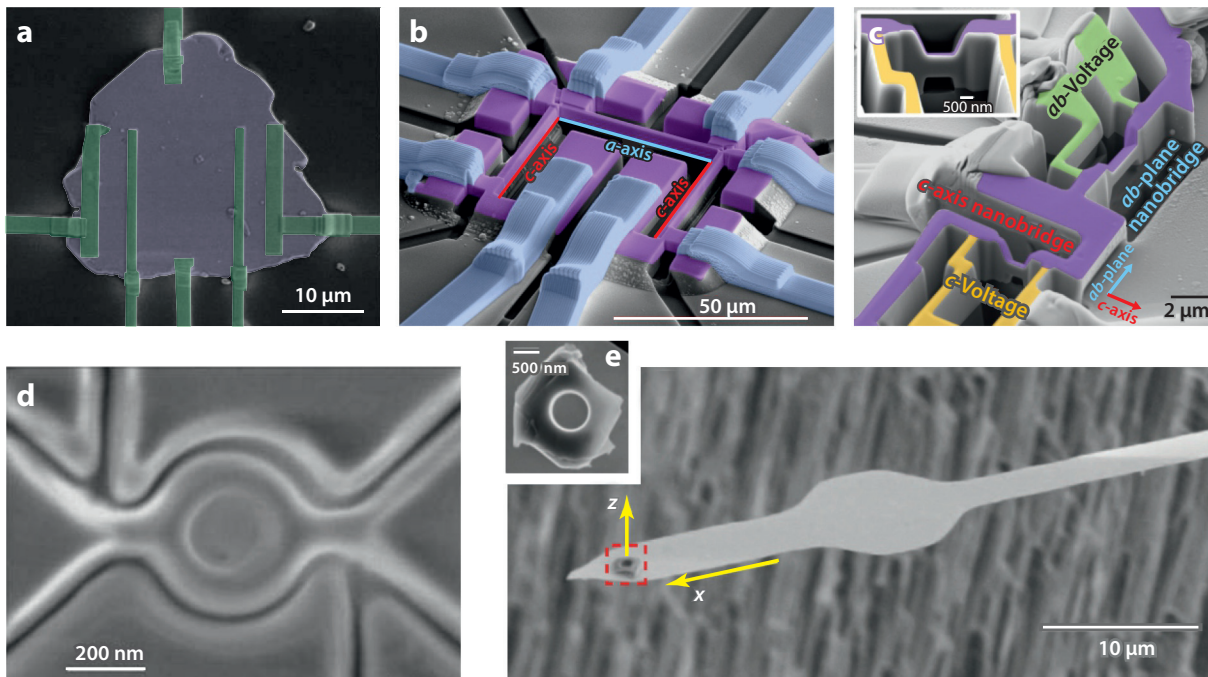


Figure 1

Examples of FIB structuring as a versatile tool to fabricate mesoscopic devices from quantum matter. (a) NdFeAs(O,F) single-crystal microplatelet contacted by FIB platinum deposition for resistivity and Hall measurements. Reproduced from Reference 26 with permission. (b) U-shaped structure of CeRhIn₅ featuring three resistance bars in series, along well-defined crystal directions. Reproduced from Reference 27 with permission. (c) microbridge of SmFeAs(O,F) featuring two necked-down freestanding crystalline bridges with a cross section of only 500 nm × 500 nm for critical current measurements along and perpendicular to FeAs layers. Reproduced from Reference 28 with permission. (d) FIB defined freestanding microring machined into a suspended graphene sheet. Reproduced from Reference 29 with permission. (e) Microcrystal of the unconventional superconductor Sr₂RuO₄ featuring an FIB-patterned hole mounted onto a cantilever for vortex torque experiments. Reproduced from Reference 20 with permission. Abbreviation: FIB, focused ion beam.

the shape and size of the microparticles in the “1111” class. The FIB played a vital role in addressing these issues. A new fabrication process, borrowing ideas from the TEM lamella preparation, was developed to fabricate crystalline microstructures for transport experiments parallel and perpendicular to the FeAs layers, thus providing the first access to out-of-plane resistivity in a true four-probe resistance bar configuration on the micrometer scale (28). Alternative approaches to assess interlayer transport involved strategies borrowed from the fabrication of intrinsic Josephson stacks in cuprates, such as the FIB-based s-shaped stack design (35, 36) and the top-mesa design using broad-beam argon (Ar)-ion milling (37).

Another powerful characteristic of FIB as a maskless micromachining technique is the miniaturization of traditional approaches to experiments under extreme conditions where sample space is very limited, such as transport in diamond anvil cells or in the small bores of pulsed-field magnets capable of reaching magnetic fields on the order of 100 T. In particular, the mechanical and electrical stability of FIB microstructures ideally addresses the main challenges of pulsed fields: It minimizes induced voltages through microscopic open-loop areas, strongly reduces eddy current heating as the sample dimension is in the micrometer range, and minimizes mechanical vibrations and magnetic torque effects through the structures’ solid connection to a larger chip

substrate. This allowed study of the superconducting anisotropy of $\text{SmFeAs}(\text{O}_{0.8}\text{F}_{0.2})$ (28) and $\text{NdFeAs}(\text{O}_{0.7}\text{F}_{0.3})$ (26) in fields up to 65 T, which suggested these materials may be used in high magnetic field applications. Furthermore, critical currents through individual grain boundaries can be determined by combining microanalytical probes and FIB patterning, thus fabricating a nanobridge exactly at a naturally occurring grain boundary in thin films (38–40).

By machining down single crystals to the submicrometer level, new experiments based on nonequilibrium transport or strong electric fields become feasible even in exotic quantum matter. For example, determining the critical current density of superconductors from transport measurements on single crystals is virtually impossible. Impractically large currents are required to reach the extreme current densities ($>10^6$ A/cm²) necessary to depin vortices in strong type-II superconductors in macroscopic crystals, which leads to severe self-heating. To circumvent this problem, FIB microbridges with cross sections smaller than 0.5 μm^2 can be tailored into a crystal structure. This approach was successfully used to determine the transport critical currents in iron arsenides, such as $\text{SmFeAs}(\text{O},\text{F})$ (28) and $(\text{Ca},\text{La})\text{FeAs}_2$ (41).

The insulating temperature dependence observed for c -direction conductivity in all members of the “1111” class hints at the possibility of intrinsic Josephson junctions within the crystal unit cell. FIB-tailored crystal devices have enabled direct measurements of the critical currents along the c -axis and uncovered a remarkable transition within the vortex system of $\text{SmFeAs}(\text{O},\text{F})$ at an intermediate temperature of $T^* \sim 42$ K below $T_c \sim 50$ K (42). A striking increase of the flux flow voltage below T^* indicates the onset of a transition of Abrikosov vortices to Josephson vortices locked in between two adjacent FeAs layers. This was further supported by vortex commensurability oscillations at T^* , suggesting that $\text{SmFeAs}(\text{O},\text{F})$ is a rare borderline case in between anisotropic 3D superconductors and weakly coupled intrinsic Josephson systems such as the most anisotropic cuprates (43).

These results fueled the experimental search for true intrinsic Josephson coupling in iron arsenides in cases in which FeAs layers are more effectively decoupled. Later, flux flow measurements on FIB structures of $(\text{Sr}_2\text{V}_4\text{O}_6)\text{Fe}_2\text{As}_2$ revealed an oscillatory dependence of the c -axis critical current on the strength of well-aligned in-plane magnetic fields, which are considered a hallmark feature of intrinsic Josephson systems (44) and are observed in textbook cases such as the high- T_c cuprate $\text{Bi}_2\text{Sr}_2\text{CaCu}_2\text{O}_{8+y}$ (45) (**Figure 2**). The identifying feature of these oscillations is their frequency dependence on the lateral width of the Josephson junction, which is given by the physical width of the device. Here the FIB opens a new approach to transport experiments on the mesoscale in which the crystal size is tuned across a relevant length scale for the physical problem. Experiments are based on alternating measurements and FIB machining steps: Thus, a device of any desired shape is thinned down in small steps using the FIB and then successively measured at each width. This FIB method to experimentally determine size dependences of resistivity has also recently been employed to observe hydrodynamic corrections to resistance scaling in ultraclean metals (46).

2. FOCUSED ION BEAM FABRICATION OF TRANSPORT DEVICES

The goal of this section is to introduce the processes of FIB transport device fabrication to enable readers to better understand the features of the technique as well as to provide a starting point for new FIB processing ventures. The focus is on an adaptation of the TEM lamella process that has proven successful in a wide range of quantum materials and is sketched in **Figure 3**.

In this adaptation of the TEM lamella process, a well-defined transport device is fabricated onto a silicon chip from an arbitrarily shaped crystal. First, a coarse rectangular bar of the desired device dimensions is precut from the crystal. Here the analytical capabilities of dual-beam FIB

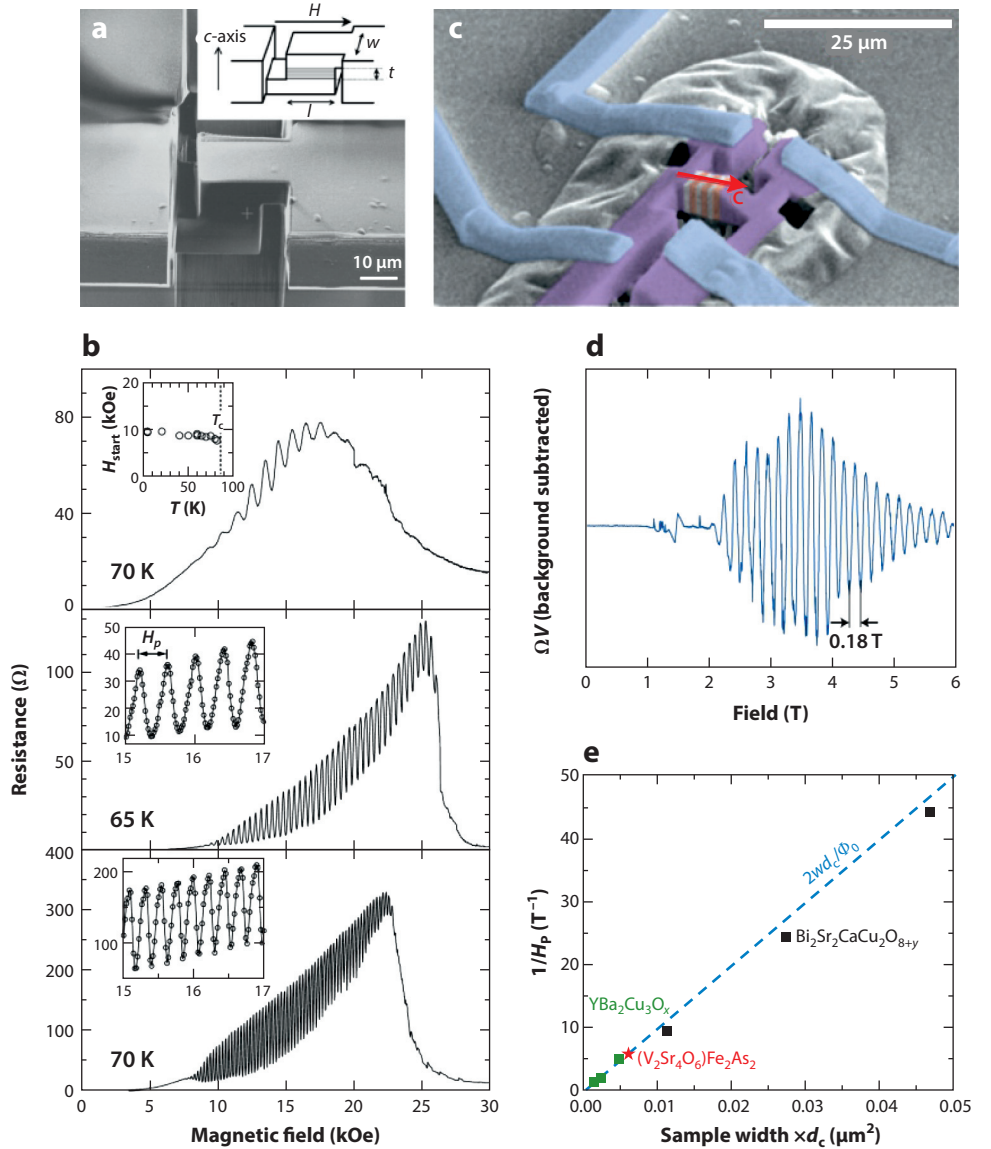


Figure 2

Mesoscale structures for intrinsic Josephson physics. (a) Bi₂Sr₂CaCu₂O_{8+y} S-type mesa structure FIB fabricated at different widths to probe (b) the finite size dependence of the vortex commensurability oscillations, thus directly evidencing intrinsic Josephson junctions (45). (c) FIB-carved out-of-plane transport bar of the iron-arsenide V₂Sr₄O₆Fe₂As₂ showing (d) commensurability oscillations that are in (e) quantitative agreement with cuprates, thus evidencing that both classes support similar intrinsic Josephson junctions (47). Panels a and b adapted from Reference 45 with permission. Panels c–e adapted from Reference 47 with permission. Abbreviation: FIB, focused ion beam.

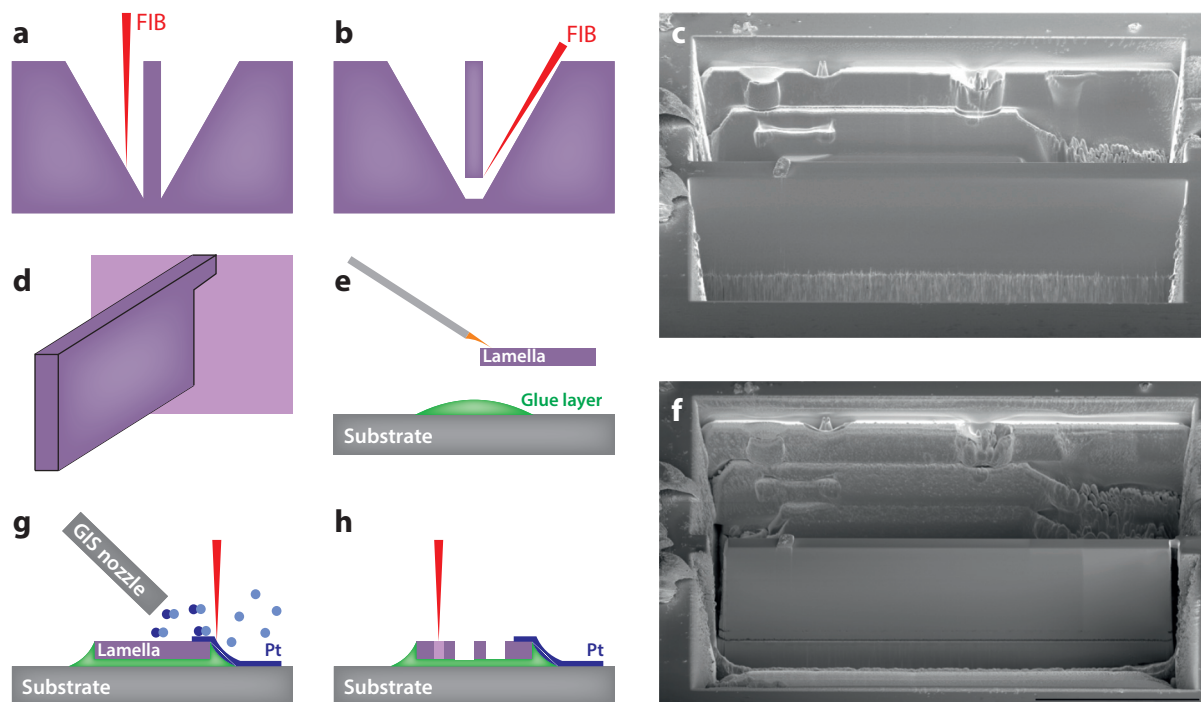


Figure 3

Transport lamella process. (a) Coarse trench cutting of a freestanding slab of the desired transport device depth. (b) Undercutting to free the slab from the parent crystal. (c) SEM image of a typical lamella after the step described in panel a. This large lamella is 150- μm long and 25- μm deep. (d) Three-dimensional representation of the undercut lamella connected to the parent crystal by a thin bridge. (e) Transfer of lamella using a micromanipulator onto chip substrate. (f) Typical SEM image of the undercut lamella sketched in panel d. (g) Fabrication of electrical contacts. (h) Fine structuring into desired final device geometry. Abbreviations: FIB, focused ion beam; GIS, gas injection system; Pt, platinum; SEM, scanning electron microscopy.

scanning electron microscopies (SEMs) such as electron backscatter diffraction, energy-dispersive X-ray spectroscopy, and high-resolution SEM are most helpful in identifying the ideal spot on the parent crystal for the lamella fabrication. Afterward, the lamella is freed from the crystal by undercutting, which involves FIB milling at a high angle ($>50^\circ$) to the surface. Here the slab is completely cut free except for a narrow ($\sim 1\ \mu\text{m}$) bridge at the corner to hold it in place (**Figure 3d,f**). Depending on the importance of surface quality, a low-voltage FIB polishing step or an ex situ surface treatment (see the section titled Ion Beam Surface Damage) may be performed at this stage. The lamella can now be extracted using a micromanipulator either in situ similar to the process of lamella transfer to a TEM grid or ex situ under an optical microscope. In the ex situ process, the lamella is freed by a gentle push with a microneedle made from an electrostatically attractive material such as Kapton. The lamella is then transferred onto a substrate where suitable electric contact pads have been prefabricated by conventional lithography. Typically, the lamella is mounted in a thin layer of glue to hold it in position and to provide a smooth slope to the lamella surface. If done carefully, the surface tension will ensure the lamella stays afloat on the glue, which should be heat-treated until water and lightweight solvents are completely evaporated. For most epoxy glues, temperatures above 140°C at 1-h cure time in vacuum have been sufficient. Now the sample can be reintroduced into the FIB chamber to fabricate electric contacts and for final device structuring.

The FIB process has a variety of key parameters that must be optimized for each material. The most obvious are the beam voltage and current. Unlike beam voltage, beam current usually has only negligible influence on the surface damage (48). The main physical influence of higher currents is an increase in sample temperature through increased power dissipation. Nevertheless, local temperature at the beam spot can sometimes decrease because higher currents require wider apertures, thus spreading the ion flux over a larger area.

2.1. Ion Beam Surface Damage

As expected for any technique involving energetic ions, the FIB damages the material's surface. Here the FIB induced surface damage is reviewed in the specific context of microfabrication of transport devices. Ion-matter interactions can cause a variety of defects, and which type of defect occurs is strongly energy dependent. At high kinetic energies, the ion penetration depth can be very long, leading to implantation of the ion as well as deposition of the beam energy in the sample and, hence, dislocation defects deep inside the material bulk. Most common FIB systems operate at acceleration voltages up to 30 kV and use Ga^{2+} ions, thus limiting the kinetic energy to 60 keV. At these comparatively low energies, the ion mean free path in metals is on the atomic length scale, and typical effective stopping distances are in the 10-nm range. Therefore, the ions and all their kinetic energy are absorbed directly in a thin surface layer, which leads to high sputter yields rendering FIB irradiation an effective tool for micromachining.

FIB-prepared structures are completely surrounded by a shell of amorphized material, but in principle, their bulk properties will be unaffected. Indeed, numerous studies of quantum materials have reported excellent agreement between measurements of transport properties in bulk and in FIB microdevices. Quantum oscillations are often visible in these structures, thus providing further strong experimental evidence of a pristine crystalline core encased in a thin amorphous shell (27, 46, 49–52). At 30 kV and grazing incidence polishing, typical damage layer thicknesses are 10–20 nm (53). Interestingly, in most cases, the amorphous layer does not gradually cross over into the crystal bulk, but instead, owing to self-annealing at room temperature, it is separated by a sharp and well-defined interface from the crystalline solid (54). Surface damage can be reduced by lowering the acceleration voltage. Typical minimal FIB voltages are on the order of 1 kV. However, operating at lower voltage limits the capability of the ion optics to focus the beam, leading to reduced imaging and milling resolution. Careful low-voltage milling can reduce the damage layer down to 3–5 nm, which is routinely achieved in FIB preparation of TEM specimens (55).

How the amorphous surface layer influences actual transport needs to be carefully investigated on a case-by-case basis. The most critical factors are the conductivity of the bulk material and the electrical contact resistance. Good quantitative understanding of conductivity in microstructures can be obtained from a parallel resistor model, acting as a current divider between the crystal bulk and the amorphous surface (49). If the bulk material is a good metal, the conductivity contribution of the heavily disordered and damaged surface layer is insignificant and corrections to bulk resistivity will be marginal. In semiconductors or insulators, however, the Ga-rich layer can contribute significantly to the device transport, as has been demonstrated in low-carrier density topological semimetals where the amorphous layer can lead to sizeable deviations from bulk conductivity (51). Another important aspect of ion-prepared surfaces is their chemical composition. Two factors are most important—Ga contamination and preferential sputtering. Amorphous layers usually contain 5–10% Ga, which may react with the constituents in the target material and form new compounds on the surface. If permitted by the structure, Ga can further diffuse into the material bulk, leading to defects and chemical potential variations deeper inside the bulk compared with the intrinsic ion stopping length.

In addition, the chemical composition of the surface damage layer can deviate significantly from that of the bulk owing to preferential sputtering. Sputter yield describes the number of sputtered target atoms per incident ion, which strongly depends on the elements present in the material. The energy scale of the sputtering process is given by the surface adhesion energy, which is highly correlated with the sublimation temperature of the material (55). This is not surprising, as the process of sublimation is the thermal equivalent process of atoms escaping from their surface potential. Therefore, if the target material is composed of elements with different sublimation temperatures, an atomic species with higher sublimation temperature will be enriched at the surface, whereas those with lower sublimation temperatures will preferentially leave the sample. A particularly extreme case was recently reported in FIB microstructures made from the Weyl semimetal NbAs. This material combines two extremes: niobium (Nb) with one of the highest sublimation temperatures of 5,017 K and arsenic (As) with a relatively low temperature of 887 K. Accordingly, the amorphous surface layer is highly As deficient with a nominal surface composition of Nb_{5.88}As. In this case, Nb enrichment due to preferential sputtering is so severe that the Nb surface layer becomes superconducting, thereby providing a novel way to fabricate proximity-effect-induced superconducting Weyl microstructures (49).

To assess the chemical properties of the damage layer quantitatively, more detailed calculations taking the thermal as well as kinetic processes into account are required. A good introductory software tool for Monte Carlo calculations of ion impact processes is the Stopping Range of Ions in Matter code (56, 57). Taking into account all secondary processes, it offers convenient simulations on the full damage cascade level and can provide quantitative insights into the energy deposition, defect and dislocation generation, the thickness of the expected damage layer, the implantation profile of Ga, and the surface composition due to preferential sputtering. It is an excellent starting point to understand computationally the surface chemistry before starting a microstructuring project.

Understanding the amorphous layer is particularly important when surface properties are essential or the intrinsic conductivity of the material is low. For example, Ga diffusion has been linked to degradations of cuprate Josephson junctions fabricated by FIB milling (58). Here, various ideas for subsequent surface treatments were successfully applied to minimize Ga contamination. A simple and often sufficient route is to subject the sample to broad-beam, high-flux, low-voltage Ar-ion milling, thus physically ablating the damage layer. Note this is a physically identical process, subject in principle to the same issues of damage formation and preferential sputtering. However, these effects are minimal at the much lower energies typically used in Ar-ion milling (~10–100 eV), which can limit the damage layer to the atomic scale. In many cases, the proper choice of ion energies can minimize the damage layer, and low-temperature annealing is effective at recrystallizing the disordered layer (59). Another route involves preferential chemical etching of the damage layer. This process can also be inverted by using chemicals that preferentially etch the undamaged material, which has been reported as an interesting route to fabricate 3D nanostructures consisting of only the amorphous layer (60). Another surface treatment route consists of thermal postfabrication annealing in vacuum (61). Owing to its tendency toward surface diffusion, Ga in the surface layer forms Ga clusters on the surface even at low temperatures (62). These Ga clusters can then be evaporated by heating the sample to 700°C in vacuum. A successive brief heat treatment in oxygen oxidizes the remaining Ga nanoparticles that did not evaporate, rendering them effectively electronically inactive.

2.2. Electric Contacts

The FIB can also be used for in situ fabrication of electric contacts to crystallites and devices. The metal deposition process, first demonstrated in 1984 (63), is based on ion-assisted chemical

vapor deposition (IA-CVD). In IA-CVD, a metal precursor gas is injected through a gas nozzle in close proximity to the sample. The precursor gas is typically a volatile metallo-organic molecule species that adsorbs on the entire surface of the sample. The impacting ions generate localized plumes of low-energy secondary electrons, which are effective at breaking the chemical bonds of the precursor gas. The lightweight organic part of the molecule is preferentially evaporated into the chamber vacuum in this kinetic process, whereas the heavier metal species contained in the precursor remains on the sample.

These deposition techniques are mainly used to fabricate capping layers protecting a surface region of interest for further ion beam-based analysis, such as TEM lamella preparation or 3D FIB tomography. However, their conductive properties have also been recognized as a versatile tool to fabricate electric contacts to micrometer-sized samples. The IA-CVD process is clearly distinct from lithography-based metallization, with unique advantages and disadvantages. First, and most importantly, IA-CVD is a maskless deposition technique that does not depend on photochemistry. The sample is not exposed to the various resist, development, and stripping chemicals typically involved in lithography. Therefore IA-CVD offers an alternative method to fabricate contacts to chemically sensitive materials. Second, without the flatness requirements of resist spincoating, corrugated and high-aspect-ratio samples can be contacted. The ion beam exposure of the contact area during the deposition process can also effectively remove surface barriers such as oxide layers, leading to reduced contact resistance compared with low-energy deposition techniques such as sputter coating or thermal deposition. For example, IA-CVD has been used to fabricate low-resistance ohmic contacts on wide classes of materials such as piezoelectric nanowires (64) and cerium- and uranium-based heavy fermion metals (27, 50).

However, compared with lithographic deposition techniques, IA-CVD contact fabrication also has inherent disadvantages. Only a limited number of gas precursors are available, with platinum, tungsten, and carbon being the most common deposits. The conductivities of IA-CVD-deposited metals are significantly lower than those of elementary metals owing to the high impurity content of organic molecules from the precursor gas. In addition, nonlinear conductivity and Schottky-diode behavior can be observed in as-grown IA-CVD contacts (65). If low conductivity and ohmic behavior is required, postannealing the contacts at elevated temperatures in an oxygen environment significantly enhances the conductivity and linearity of such deposits (66–69). In addition, IA-CVD commonly leads to deposition outside of the irradiated region owing to the generation of highly reactive, only partially decomposed molecules. This so-called halo or overspray is less conductive than the primary deposit but can still cause cross talk and leakage current in low-conductivity devices. In cases in which ion beam exposure to the device must be minimized, electron-assisted CVD is also possible. The resulting films are more resistive owing to their higher carbon content and the accordingly lower density of percolating paths between the metal nanoclusters, but electron-beam deposits can also be improved through annealing approaches (70).

In addition, IA-CVD can fabricate superconducting materials, thus opening the possibility of in situ fabrication of quantum-coherent superconducting devices from unconventional materials. The most common precursor gas for superconducting materials is $\text{W}(\text{CO})_6$. These deposits exhibit type-II superconductivity with comparatively high $T_c \sim 5\text{--}6\text{ K}$, and their superconducting properties are reliable and robust with little dependence on the processing parameters. For special applications, fine-tuning of the deposition parameters may be required to achieve high critical fields, critical currents, or low normal state resistivity (71). Higher transition temperatures up to 11 K (onset) can be achieved under special circumstances in carbon deposits fabricated from phenanthrene precursor gas (72). Interestingly, despite the amorphous and granular nature of such deposits, a uniform s-wave gap on the atomic-scale and a hexagonal vortex pattern has been

observed by scanning tunneling microscopy (73). Depending on the surface chemistry, conductivity, scale, and purpose of the microstructuring project, IA-CVD or traditional lithographic techniques may be preferable. In the following section, general strategies for growth of high-quality electrical contacts are discussed.

2.3. Ion-Assisted Chemical Vapor Deposition Strategies for Quantum Materials

A challenge in fabricating contacts to devices based on crystals of quantum materials is overcoming the height step between the flat substrate and the crystal to form an ohmic, low-resistance electric contact. Owing to a self-shadowing effect known as terrace formation, the most straightforward approach to connect the substrate to the crystal usually results in poorly conducting or electrically disconnected deposits (**Figure 4a,e**). As the deposit grows on top of the crystal, terraces extruding outward prevent the ion beam from reaching the surface of the substrate underneath, thus self-inhibiting the growth process. Once formed, these terraces do not self-heal but continue to grow outward, and even very thick metal deposits will not provide a continuous conductive path. This can be partially mitigated by going to a higher angle of incidence, yet electrically poor connections remain typical for this approach. Two strategies have proven very successful. The first consists of a two-step process in which a series of deposits is grown at 1–2- μm lateral distance from the crystal to form a smooth connection from the substrate base to the top of the crystal (**Figure 4d,g**). Once the staircase reaches the height of the crystal, the gap is bridged to form a good conductive connection between the metallic staircase and the crystal. A common scan strategy for deposits is a meandering or serpentine pattern, which often leads to line patterns in high-current deposits. This structure leads to anisotropic conductivity of FIB-deposited platinum,

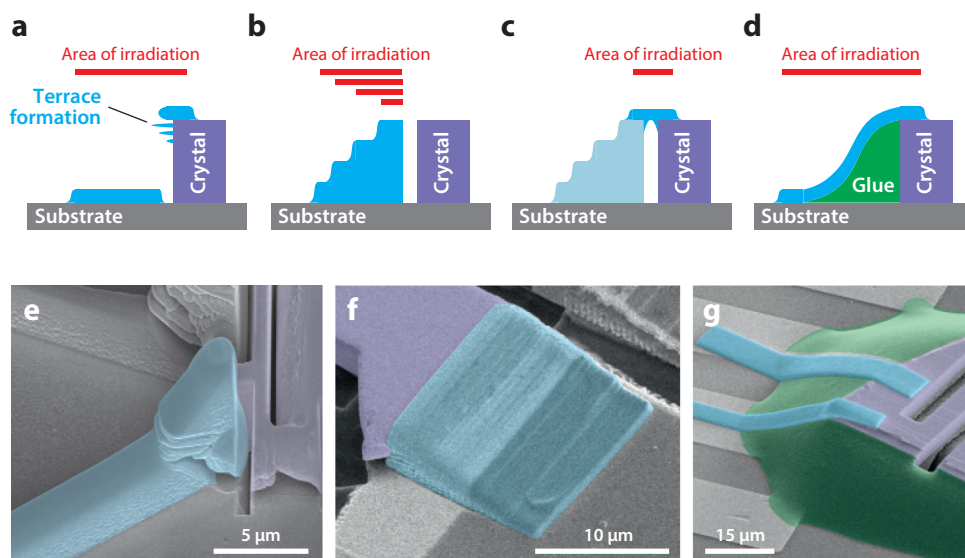


Figure 4

Overview of ion-assisted chemical vapor deposition of electric contacts. (*a–d*) Schematic drawings of various contacting strategies applied to electrically contact a thick crystal of a quantum material. Red bars indicate the area irradiated by the focused ion beam. (*e–g*) Scanning electron microscopy images of actual contacts: (*e*) typical terrace formation leading to high contact resistance, (*f*) staircase contact as sketched in panels *b* and *c*, and (*g*) top contact deposited over glue.

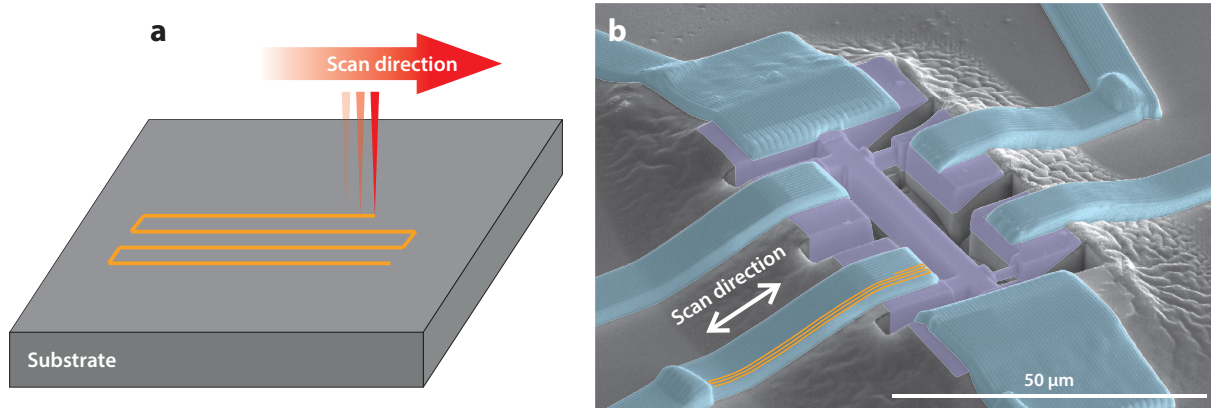


Figure 5

Scan direction for contact fabrication across steep sidewalls. (a) Sketch of a typical serpentine scan strategy. The resulting deposit is anisotropic in connectivity and conductivity. The scan direction should be perpendicular to the obstacle. (b) Scanning electron microscopy image of a crystal microstructure contacted via the process described in panel a. Scan direction and beam guidance are highlighted. Note the line structure in the platinum deposits (blue).

with highest conductivity along the lines (shown in **Figure 5**). Contact patterns should thus always be aligned so that the lines are along the intended flow of current. Line formation could easily be suppressed by a smaller pitch between spots at lower currents or by alternating the direction of the scan; however, line structure has proven advantageous for reliability and thermal cycling stability.

When the crystal tolerates the solvents and chemistry encountered in epoxy resin, a very successful strategy can be glue mounting (**Figure 4b,c,f**). In this approach, the crystal is floated on a microscopic droplet of glue, which naturally provides a smooth slope between crystal top and substrate. This eliminates the main issue of steep vertical steps, and high-quality contacts can be easily grown. The key to successful deposition is a well-cured and water-free epoxy glue. Water dissociates under ion irradiation to form an effective etching agent, thus successfully inhibiting growth of IA-CVD deposits (74).

3. POTENTIAL AND OUTLOOK

With the widespread availability of high-quality Ga-FIB machines, new applications, material classes, and structure designs for quantum matter are being explored every day. Yet, upcoming technological changes will also strongly impact the direction of microstructured quantum matter. Two emerging FIB technologies have been commercialized in recent years, and with their increasing availability, exciting new opportunities for microstructuring of quantum matter will emerge. New instruments include plasma FIB and helium/neon (He/Ne) FIB.

The maximal current for well-focused beams on Ga LMIS FIB is fundamentally limited. Increasing its beam current beyond 5–10 nA leads to significant divergence of the beam spot due to aberrations, and the maximal attainable current is fundamentally limited to approximately 100 nA owing to a breakdown of the Taylor cone at high extraction voltages. The probe current is directly proportional to the material removal rate, and thus Ga LMIS FIB technology is inconveniently slow for large volume removal (**Figure 6**). This issue is addressed by plasma FIB technology. It is based on radio-frequency generation of xenon (Xe) plasma, accelerated by an extraction voltage and collimated through an aperture. This source maintains a power law emission even at high

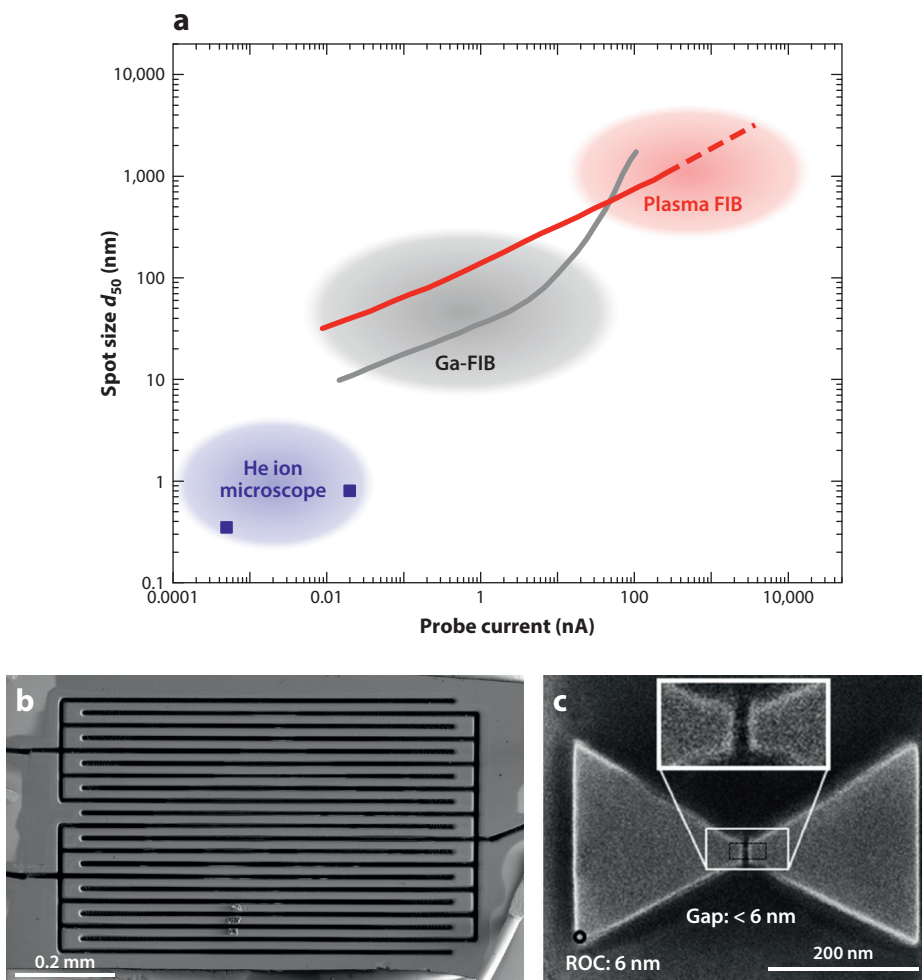


Figure 6

Comparison of FIB-microstructuring technologies. (a) d_{50} denotes the effective central beam diameter containing 50% of the ion current, and the probe current is proportional to the sputter rate. Ga LMIS excels in the intermediate range of spot sizes between 10 and 1,000 nm, but significant loss of focus occurs as the current is increased to the limit of the source emission around 100 nA (gray line) (75). Finer spots at significantly higher currents can be achieved by xenon plasma FIB (red line) (75). Current state-of-the-art developments have pushed the achievable emission currents into the 2,000-nA range (dashed red line). The He ion microscope can deliver ultrasmall spot sizes well below 1 nm, yet the source technology is limited to relatively low extraction currents (blue points) (estimated following Reference 76). (b) Large-scale crystal of YbRh_2Si_2 structured into a 15.6-mm-long, but only 15- μm -wide, microwire in under 2 h without detectable deterioration of crystal quality. (c) Gold nanoresonator defined by a He ion microscope and with an electric field gap smaller than 6 nm. Reprinted with permission from H. Kollmann et al., *Nano Lett.* 14:4778–84. Copyright 2014 American Chemical Society, Reference 77). Abbreviations: FIB, focused ion beam; Ga, gallium; He, helium; LMIS, liquid metal ion source; ROC, radius of curvature.

currents, leading to a much slower increase in spot diameter with increasing currents (75). Therefore, at high ion currents greater than 10 nA, plasma FIB provides significantly better resolution at the same current and is capable of delivering highly focused ion beam currents above 2,000 nA. Thus, the time to remove large volumes of material is dramatically reduced, and entirely new regions of macroscopic quantum materials structured with micrometer precision become accessible, for example, for quantum matter photonic crystals or large-scale resistive devices in which an entire as-grown crystal is shaped into a resistive meander shape (**Figure 6**). This technology will bridge the gap between the macroscale and the mesoscale, and significantly impact the field by improving the economics of FIB micromachining. At present, the fabrication schemes discussed in this article typically involve 10 hours of valuable Ga-FIB time, with the most time spent for large volume material removal on the 10- μm scale. At the same spot size, plasma FIB can output exponentially higher ion currents and thus reduce the required time for sample fabrication to less than 1 h. Xe also has chemical advantages, as it neither implants into the surface nor chemically reacts with the material. The generated surface damage layer at equal acceleration voltage is also significantly smaller for Xe compared with Ga (for example, 41% smaller in silicon) owing to its higher atomic mass (78).

He/Ne ion microscopes push the boundaries for FIB micromachining into the nanometer range, achieving ultimate resolution at low ion currents (79). The basic idea is to localize the source emission down to the atomic level by preparing a tilted three-atomic trimer tip of a tungsten needle and canting one of the atoms closer to the extraction electrode. Under ideal conditions, this adaptation of a field ion microscope features a single tungsten atom acting as a high-brightness source ionizing He or Ne (for a good overview of He ion microscopy technology, see 76). The atomic scale limits the current emission capabilities to approximately 150 pA. With their high spatial resolutions, He ion microscopes are ideally suited for ultrahigh-resolution imaging and have been successfully used to fabricate nanostructures such as plasmonic nanoresonators (77, 80, 81), nanoscale magnetic domains (82), or direct-write Josephson junctions in YBCO (83). One critical difference between He and heavier ions such as Ga or Xe is its significantly increased mean free path in matter. Its long penetration depth leads to stronger bulk material damage and implantation of He into the target material in the 100-nm range (84).

These new developments will certainly impact quantum materials research in exciting ways. By combining these new technologies, 3D single-crystal microstructures with feature sizes ranging from the macroscopic world to the atomic limit of the unit cell will become feasible. Finite size effects influencing the electronic properties of quantum matter on the mesoscale can be directly studied, and the interplay of size and shape for the electronic structure may lead to novel phenomena in quantum matter similar to the spectacular behavior of metamaterials made from common metals. As we are just beginning to introduce these technologies into research in quantum materials, it will be most exciting to see how the true potential of future FIB-based techniques unfolds.

DISCLOSURE STATEMENT

The author is not aware of any affiliations, memberships, funding, or financial holdings that might be perceived as affecting the objectivity of this review.

LITERATURE CITED

1. Krohn VE, Ringo GR. 1975. *Appl. Phys. Lett.* 27:479–81
2. Seliger RL, Ward JW, Wang V, Kubena RL. 1979. *Appl. Phys. Lett.* 34:310–12

3. Orloff J, Utlaut M, Swanson L. 2003. *High Resolution Focused Ion Beams: FIB and Its Applications*. New York: Springer Sci. Bus.
4. Gierak J. 2009. *Semicond. Sci. Technol.* 24:43001
5. Ishitani T, Yaguchi T. 1996. *Microsc. Res. Tech.* 35:320–33
6. Uchic MD, Dimiduk DM, Florando JN, Nix WD. 2004. *Science* 305:986–89
7. Chen F. 2012. *Laser Photonics Rev.* 6:622–40
8. Narayan K, Subramaniam S. 2015. *Nat. Methods* 12:1021–31
9. Latyshev YI, Yamashita T. 1999. *Phys. Rev. Lett.* 82:5345–48
10. Kadowaki K, Kakeya I, Yamamoto T, Yamazaki T, Kohri M, Kubo Y. 2006. *Phys. C* 437–38:111–17
11. Kim SJ, Latyshev YI, Yamashita T. 1999. *Appl. Phys. Lett.* 74:1156–58
12. Simon RW, Bulman JB, Burch JF, Coons SB, Daly KP, et al. 1991. *IEEE Trans. Magn.* 27:3209
13. Nagel J, Konovalenko KB, Kemmler M, Turad M, Werner R, et al. 2011. *Supercond. Sci. Technol.* 24:15015
14. Sandhu A, Masuda H, Kurosawa K, Oral A, Bending SJ. 2001. *Electron. Lett.* 37:524–27
15. Stanishvsky A, Aggarwal S, Prakash AS, Melngailis J, Ramesh R. 1998. *J. Vac. Sci. Technol. B* 16:3899–902
16. Lobo DE, Banerjee PC, Easton CD, Majumder M. 2015. *Adv. Energy Mater.* 5:1500665
17. Nagase M, Takahashi H, Shirakawabe Y, Namatsu H. 2003. *Jpn. J. Appl. Phys.* 42:4856–60
18. Du H, Degraeve JP, Xue F, Liang D, Ning W, et al. 2014. *Nano Lett.* 14:2026–32
19. Zhang Y, Hui C, Sun R, Li K, He K, et al. 2014. *Nanotechnology* 25:135301
20. Jang J, Ferguson DG, Vakaryuk V, Budakian R, Chung SB, et al. 2011. *Science* 331:186–88
21. Nago Y, Shinozaki T, Tsuchiya S, Ishiguro R, Kashiwaya H, et al. 2016. *J. Low Temp. Phys.* 183:292–99
22. Kambara H, Kashiwaya S, Kashiwaya H, Tanaka Y, Maeno Y. 2011. *Phys. C* 471:708–10
23. Kashiwaya S, Kambara H, Kashiwaya H, Furuta T, Yaguchi H, et al. 2010. *Phys. C* 470:S736–37
24. Kambara H, Kashiwaya S, Yaguchi H, Asano Y, Tanaka Y, Maeno Y. 2009. *Phys. C* 469:1030–33
25. Kashiwaya S, Kashiwaya H, Kambara H, Furuta T, Yaguchi H, et al. 2011. *Phys. Rev. Lett.* 107:77003
26. Jaroszynski J, Hunte F, Balicas L, Jo Y, Raicevic I, et al. 2008. *Phys. Rev. B* 78:174523
27. Moll PJW, Zeng B, Balicas L, Galeski S, Balakirev FF, et al. 2015. *Nat. Commun.* 6:6663
28. Moll PJW, Puzniak R, Balakirev F, Rogacki K, Karpinski J, et al. 2010. *Nat. Mater.* 9:628–33
29. Lucot D, Gierak J, Ouerghi A, Bourhis E, Faini G, Mailly D. 2009. *Microelectron. Eng.* 86:882–84
30. Stewart GR. 2011. *Rev. Mod. Phys.* 83:1589–652
31. Luo HQ, Cheng P, Wang ZS, Yang H, Jia Y, et al. 2009. *Phys. C* 469:477–84
32. Pisoni A, Katrych S, Arakcheeva A, Verebelyi T, Bokor M, et al. 2016. *Phys. Rev. B* 94:24525
33. Katrych S, Rogacki K, Pisoni A, Bosma S, Weyeneth S, et al. 2013. *Phys. Rev. B* 87:180508(R)
34. Pisoni A, Katrych S, Szirmai P, Náfrádi B, Gaál R, et al. 2016. *J. Phys. Condens. Matter* 28:115701
35. Shirai K, Kashiwaya H, Miura S, Ishikado M, Eisaki H, et al. 2010. *Phys. C* 470:1473–76
36. Kashiwaya H, Shirai K, Matsumoto T, Shibata H, Kambara H, et al. 2010. *Appl. Phys. Lett.* 96:202504
37. Müller P, Koval Y, Lazareva I, Steiner C, Wurmehl S, et al. 2016. *Phys. Status Solidi B* 254:1600157
38. Hong S-H, Lee S-G, Jung S-G, Kang WN. 2012. *J. Korean Phys. Soc.* 61:1430–34
39. Hong S-H, Lee NH, Kang WN, Lee S-G. 2014. *Supercond. Sci. Tech.* 27:55007
40. Li J, Ji M, Schwarz T, Ke X, Van Tendeloo G, et al. 2015. *Nat. Commun.* 6:7614
41. Cagliaris F, Sala A, Fujioka M, Hummel F, Pallecchi I, et al. 2016. *APL Mater.* 4:20702
42. Moll PJW, Balicas L, Geshkenbein V, Blatter G, Karpinski J, et al. 2013. *Nat. Mater.* 12:134–38
43. Moll PJW, Balicas L, Zhu X, Wen H-H, Zhigadlo ND, et al. 2014. *Phys. Rev. Lett.* 113:186402
44. Koshelev A. 2007. *Phys. Rev. B* 75:214513
45. Ooi S, Mochiku T, Hirata K. 2002. *Phys. Rev. Lett.* 89:247002
46. Moll PJW, Kushwaha P, Nandi N, Schmidt B, Mackenzie AP. 2016. *Science* 351:1061–64
47. Moll PJW, Zhu X, Cheng P, Wen H-H, Batlogg B. 2014. *Nat. Phys.* 10:644–47
48. Rubanov S, Munroe PR. 2004. *J. Microsc.* 214:213–21
49. Bachmann MD, Nair N, Flicker F, Ilan R, Meng T, et al. 2017. *Sci. Adv.* 3:e1602983
50. Harrison N, Moll PJW, Sebastian SE, Balicas L, Altarawneh MM, et al. 2013. *Phys. Rev. B* 88:241108
51. Moll PJW, Nair NL, Helm T, Potter AC, Kimchi I, et al. 2016. *Nature* 535:266–70
52. Moll PJW, Potter AC, Nair NL, Ramshaw B, Modic K, et al. 2016. *Nat. Commun.* 7:12492
53. Kato NI. 2004. *J. Electron Microsc.* 53:451–58
54. Kato NI, Kohno Y, Saka H. 1999. *J. Vac. Sci. Technol. A* 17:1201

55. Giannuzzi LA, Stevie FA. 1999. *Micron* 30:197–204
56. Ziegler JF. 2004. *Nucl. Instrum. Methods Phys. Res. B* 220:1027–36
57. Ziegler JF, Ziegler MD, Biersack JP. 2010. *Nucl. Inst. Methods Phys. Res. B* 268:1818–23
58. Warburton PA, Fenton JC, Korsah M, Grovenor CRM. 2006. *Supercond. Sci. Technol.* 19:S187–90
59. Cooper D, Ailliot C, Barnes J, Hartmann J, Salles P, et al. 2010. *Ultramicroscopy* 110:383–89
60. Llobet J, Sansa M, Borrisé X, Pérez-Murano F, Gerbolés M. 2015. *J. Micro/Nanolithogr. MEMS MOEMS* 14:31207
61. Schilling A, Adams T, Bowman RM, Gregg JM. 2007. *Nanotechnology* 18:35301
62. Mikkelsen A, Hilner E, Andersen J, Ghatnekar-Nilsson S, Montelius L, Zakharov A. 2009. *Nanotechnology* 20:325304
63. Gamo K, Takakura N, Samoto N, Shimizu R, Namba S. 1984. *Jpn. J. Appl. Phys.* 23:293–95
64. Lu MP, Song J, Lu MY, Chen MT, Gao Y, et al. 2009. *Nano Lett.* 9:1223–27
65. Motayed A, Davydov AV, Vaudin MD, Levin I, Melngailis J, Mohammad SN. 2006. *J. Appl. Phys.* 100:24306
66. De Teresa JM, Cárdoma R, Fernández-Pacheco A, Montero O, Strichovanec P, Ibarra MR. 2009. *J. Nanomater.* 2009:936863
67. Fang J-Y, Qin S-Q, Zhang X-A, Liu D-Q, Chang S-L. 2014. *Chin. Phys. B* 23:88111
68. Mulders JLL. 2014. *Appl. Phys. A* 117:1697–1704
69. Reguer A, Bedu F, Tonneau D, Dallaporta H, Prestigiacomo M, et al. 2008. *J. Vac. Sci. Technol. B* 26:175–80
70. Van Dorp WF, Hagen CW. 2008. *J. Appl. Phys.* 104:81301
71. Li W, Fenton JC, Wang Y, McComb DW, Warburton PA. 2008. *J. Appl. Phys.* 104:93913
72. Dhakal P, McMahon G, Shepard S, Kirkpatrick T, Oh JI, Naughton MJ. 2010. *Appl. Phys. Lett.* 96:262511
73. Guillamón I, Suderow H, Vieira S, Fernández-Pacheco A, Sesé J, et al. 2008. *New J. Phys.* 10:93005
74. Utke I, Hoffmann P, Melngailis J. 2008. *J. Vac. Sci. Technol. B* 26:1197
75. Smith NS, Skoczylas WP, Kellogg SM, Kinion DE, Tesch PP, et al. 2006. *J. Vac. Sci. Technol. B* 24:2902
76. Hlawacek G, Götzhäuser A. 2016. *Helium Ion Microscopy*. New York: Springer
77. Kollmann H, Piao X, Esmann M, Becker SF, Hou D, et al. 2014. *Nano Lett.* 14:4778–84
78. Kelley RD, Song K, Van Leer B, Wall D, Kwakman L. 2013. *Microsc. Microanal.* 19(Suppl. 2):862–63
79. Ward BW, Notte JA, Economou NP. 2006. *J. Vac. Sci. Technol. B* 24:2871
80. Melli M, Polyakov A, Gargas D, Huynh C, Scipioni L, et al. 2013. *Nano Lett.* 13:2687–91
81. Wang Y, Abb M, Boden SA, Aizpurua J, De Groot CH, Muskens OL. 2013. *Nano Lett.* 13:5647–53
82. Röder F, Hlawacek G, Wintz S, Hübner R, Bischoff L, et al. 2015. *Sci. Rep.* 5:16786
83. Cybart SA, Cho EY, Wong TJ, Wehlin BH, Ma MK, et al. 2015. *Nat. Nanotechnol.* 10:598–602
84. Smith DA, Joy DC, Rack PD. 2010. *Nanotechnology* 21:175302